

# Size-Density Spectra and their Application to Image Classification

Igor Zingman, Ron Meir, Ran El-Yaniv\*

December 26, 2005

## Abstract

In this paper we develop a density opening operator that is shown to satisfy the properties of an algebraic opening. This density opening enables the development of a number of variants of pattern spectra, which quantify the size or density information of a blob arrangement within the image. In contrast to regular morphological pattern-size spectra, the proposed pattern spectra are spatially sensitive and robust to noise distortions. A size-density signature was introduced and used for solving image classification tasks. Application of the pattern size density spectrum to the classification of real world medical images is illustrated.

## 1. Introduction

A pattern spectrum is a powerful tool for analyzing the size–shape content of an image. It quantifies the distribution of object sizes in an image relative to some predefined shape called a structuring element [1]. Fig. 2 shows examples of pattern spectra corresponding to the images in Fig. 1. The pattern spectrum originated from the mor-

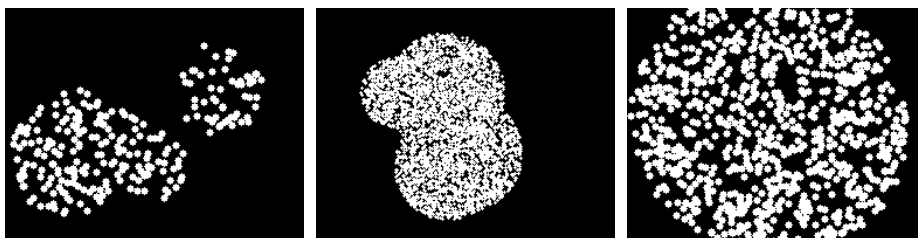


Figure 1: Artificial images of clustered objects.

phological granulometries developed by Matheron [13] to study the distribution of pore

---

\*This work is partially supported by the Ministry of Science Infrastructure grant number 01-01-01499 and by the Ollendorff Research Fund

sizes in porous media. Further, size distributions have been extensively used in quantitative analysis of biological and geological sections captured on microscopic images [8]. Much work has also utilized the granulometry tool for texture discrimination (see, for example [7, 12]). The pattern spectrum is computed by measuring the difference

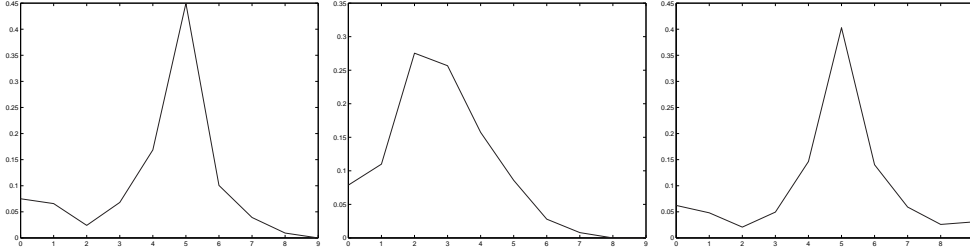


Figure 2: Pattern spectra of images shown in Fig.1 .

between opened images obtained using increasing structuring element. Usually, the measure of the image difference is simply the area of the difference image. The computation scheme for pattern spectra resembles the Laplacian pyramid for multiscale image analysis [14], with the essential difference that the filtering operator associated with pattern spectra is non-linear.

There are number of drawbacks to classical pattern spectra, one of which is that the opening operator used to build the pattern spectrum is sensitive to image noise. When a binary image contains a large object, even spatially sparse noise can drastically change the pattern spectrum. Such image noise divides the object into smaller parts and the opening operator then captures only these smaller shapes. Consequently, the pattern spectrum is shifted to lower size values. Some solutions have already been proposed in order to increase the robustness of morphological filtering in noisy environments, including soft erosions and soft dilations [10]. Standard definitions were relaxed in such way that some degree of robustness was achieved. This required the definition of two structuring elements, a core subset  $A$  and a soft subset  $A/B$ . There are no analytical criteria for choosing the relationships between these two subsets. Based on these operations, the authors also introduced soft closing and soft opening, but in fact the operators proposed do not satisfy all the properties required for opening: they are not idempotent and not anti-extensive. Other similar approaches have been proposed [6] that define openings that are robust to noise, but they also do not satisfy the basic opening properties and suffer from uncertainty in choosing extra parameters.

The other inherent drawback of the classical pattern spectrum is that it does not consider the spatial arrangement of image objects. Thus, analyzed images that contain different structures may have very similar pattern spectra; see Figs. 1 and 2, for example. Wilkinson has described an approach [5] to capture spatial information using a special variant of a spatially sensitive pattern spectrum. The author suggested quantification of the spatial distribution of the difference of opened images, instead of applying a measure such as area. Specifically, he suggested calculation of the moments of spatial distributions. In this way, we can obtain distributions of spatial moments in place of the size distributions. Although this method produces a pattern spectrum that contains spatial information, its potential for discriminating images with a variety of objects and structures is weak, since it is too hard to classify complex 2D spatial

distributions using only a number of moment descriptors. In addition, as the author has noted, additional post-processing is required to make such a pattern spectrum translation-invariant.

In this paper we propose a size–density spectrum sensitive to the relative spatial arrangement of small image shapes or blobs. We also introduce a method based on the size–density spectrum that is capable of discriminating between a large variety of noisy images that contain objects in the form of blob clusters (Fig. 1 shows examples of such primitive objects) of different sizes and densities.<sup>1</sup> The pattern size–density spectrum or image signature is obtained using a specially designed density opening operator. We show that the binary version of this operator is equivalent to the previously introduced (but still not widely used) rank-max opening [3, 4, 11]. However, no gray-scale counterpart of density opening reported in the literature.

The paper is organized as follows. Section 2 briefly describes the concepts and tools of morphological image processing. The fuzzy set framework used to pass from binary to gray-scale morphology is outlined in Section 2.2. Application of the morphological image-processing approach to the estimation of size distributions in images is presented in Section 3. The opening spectrum and top-hat spectrum are illustrated. Sections 2 and 3 define the notations used throughout the paper. Subsequent sections introduce the original concepts and approach that can be used in pattern recognition tasks. In Section 4 density opening is introduced and the relevant properties are investigated. Section 5 describes the application of the density opening operator to the generation of size–density signatures. As already noted, these signatures quantify the size and density aspects of clustered blobs within image scenes. Section 6 illustrates the combination of size–density signatures with the Support Vector Machine method for discrimination between images. Classification experiments are described for both artificial and real world images.

## 2. Principles of morphological image processing (selected topics)

### 2.1. Basic binary morphological operators

Here we review basic concepts and notations related to binary morphology. We restrict the presentation here to discrete images only. Mathematical morphology originates from set theory [13] and was originally used for the processing and analysis of binary images. A binary image is a subset of a discrete plane  $\mathbb{Z}^2$ . It is often associated to a set of white pixels, whereas its background is associated to black pixels. The binary images will be denoted by  $X$  or some other capital letter. The related morphology is called binary morphology. A structural element (SE) is usually a small simple subset of the discrete plane  $\mathbb{Z}^2$  used to probe the analyzed image. The basic operations of mathematical morphology are erosion and dilation. The translation of  $X$  by a point  $z$

---

<sup>1</sup>Such images are often encountered in medicine and biology. For example, we have used the proposed method for discrimination between breast cancer tissue specimens.

is denoted by  $X_z$  and defined by  $X_z = \{x + z \mid x \in X\}$ . The binary erosion of  $X$  by  $B$  is denoted by  $X \ominus B$  and defined as follows:

$$X \ominus B = \{z \mid B_z \subseteq X\} = \bigcap_{b \in B} X_{-b}$$

The binary dilation of  $X$  by  $B$  is denoted by  $X \oplus B$  and defined as follows:

$$X \oplus B = \{x + b \mid x \in X, b \in B\} = \bigcup_{b \in B} X_b$$

Generally, erosion shrinks image objects, whereas dilation expands them. Structural opening is another basic morphological operator. Structural opening of  $X$  by  $B$  is denoted by  $X \circ B$  and defined as erosion followed by dilation with the same structuring element:

$$X \circ B = (X \ominus B) \oplus B. \quad (1)$$

The main property of structural opening is the elimination of small image details. The opening filters out specific details that are smaller than the structuring element used. Generally, opening discards small bright regions, breaks narrow bright bridges and smoothes object contours. It can be shown that binary opening is equivalent to the union of all translated SEs fitting the analyzed set:

$$X \circ B = \bigcup_{B_x \subseteq X} B_x. \quad (2)$$

The last equation provides a deeper insight into the geometric meaning of binary opening.

The operations  $\oplus$ ,  $\ominus$ , and  $\circ$  are computed from left to right and, to simplify equations we sometimes omit extra brackets. For example,  $(X \circ B) \circ B$  is equivalent to  $X \circ B \circ B$ .

## 2.2. From binary to gray-scale morphology

A discrete gray-tone image is usually represented by a 2D function, mapping  $\mathbb{Z}^2$  to  $\mathbb{R}$ . In this work, we view a discrete gray-tone image as a corrupted version of an ideally-binary set. In this context, we prefer to represent a gray-tone image by a fuzzy set, normalized to fall in the range of  $[0,1]$ .

The morphology of gray-tone images is termed gray-scale morphology. The extension of binary operators to gray-scale counterparts is desirable, since it avoids information loss from the early setting of a threshold. There are a number of approaches used to extend the concepts of binary morphology to gray-scale morphology, including using the umbra concept to pass from 2D functions to 3D sets [15, 16] and abstract lattice theory [20, 9]. The former is a min/max approach, when union is replaced by local max and intersection is replaced by local min operations [17]. Essentially, the approaches yield similar results (for the flat structuring elements that are discussed in the next). The use of fuzzy set concepts is another elegant way to adapt binary operators to work

with gray-tone images. This approach is directly connected to the min/max strategy. It retains the same concepts of union, intersection and inclusions involved in the definition of binary operators. In this work, we adopt the fuzzy set framework to morphologically manipulate gray-tone images. First, because (as we mention above) the gray-tone images in our application are better viewed as fuzzy sets. Second, because we find it mathematically more convenient to pass from binary to gray-scale morphology using the same set of concepts. And, finally, because, in our opinion, the intuitive (geometric) meaning is clearer within this framework. It should be noted that our fuzzy approach differs from the one presented in [24],[23], where not only the images but the structuring elements are considered fuzzy. In addition, we do not make the morphological operations themselves fuzzy, as in [23].

The fuzzy set concepts used in the sequel are now briefly outlined. Let  $E$  be any reference set. A fuzzy subset  $X$  of  $E$  is a set of ordered pairs  $X = \{x, \mu_X(x)\}$ , where  $\mu_X(x)$  belongs to the interval  $[0, 1]$  and is named membership function of subset  $X$ . Every image can be represented as a fuzzy subset by rescaling the intensities to range between zero and one. Thus, the value of the membership function at pixel  $x$  will be equal to the normalized intensity of the image at  $x$ . The membership function indicates the probability that the point  $x$  is in the foreground of an image. A crisp set is a fuzzy set with membership function equals to zero or one, but not intermediate values. The binary image is represented by a crisp set. The support  $S_X$  of the fuzzy set  $X$  is a crisp set that contains elements of  $X$  with non-zero membership  $S_X = \{x | \mu_X(x) > 0\}$ . The empty fuzzy set, denoted by  $\emptyset$ , is a set with an empty support. The translation of a fuzzy set  $X$  by a point  $z$  is denoted, similar to translation of the crisp set, by  $X_z$  and is defined by  $X_z = \{x + z, \mu_X(x - z)\}$ . To compare several fuzzy sets, we use the following notations:

$$X \succ Y \quad \text{if and only if} \quad \forall x \in S_X, \quad \mu_X(x) \geq \mu_Y(x)$$

The last expression can be described as follows. We say that (fuzzy) set  $X$  contains (fuzzy) set  $Y$ , or that set  $Y$  is included in set  $X$ . Equivalently, we sometimes say that  $X$  is ‘greater’ than  $Y$  or  $Y$  is ‘smaller’ than  $X$ .

$$X \prec Y \quad \text{if and only if} \quad \forall x \in S_Y, \quad \mu_X(x) \leq \mu_Y(x)$$

$$X = Y \quad \text{if and only if} \quad \forall x \in E, \quad \mu_X(x) = \mu_Y(x)$$

The union and intersection operations are defined on fuzzy sets as follows:

$$\mu_{X \vee Y}(x) = \max(\mu_X(x), \mu_Y(x)), \quad X \vee Y = \{x, \mu_{X \vee Y}(x) \mid x \in E\},$$

$$\mu_{X \wedge Y}(x) = \min(\mu_X(x), \mu_Y(x)), \quad X \wedge Y = \{x, \mu_{X \wedge Y}(x) \mid x \in E\}.$$

In this way, the union image is simply an image of local maxima and the intersection image is an image of local minima. In the next we will use the following relations between fuzzy sets:

$$Y \vee X \succeq X \tag{3}$$

$$Y \wedge X \preceq X \quad (4)$$

$$(\bigvee_i X_i) \wedge Y = \bigvee_i (X_i \wedge Y). \quad (5)$$

The same equations certainly hold for the unions and intersections of regular crisp sets. We denote the bounded difference of two fuzzy sets by  $X - Y$ , which is defined as follows:

$$\mu_{X-Y}(x) = \max(0, \mu_X(x) - \mu_Y(x)), \quad X - Y = \{x, \mu_{X-Y}(x) \mid x \in E\}. \quad (6)$$

When  $Y \preceq X$ , the membership function  $\mu_{X-Y}$  of the set difference  $X - Y$  is simply the difference between membership functions  $\mu_X(x) - \mu_Y(y)$ . It should be noted that the definition of fuzzy set difference is usually distinct from this bounded difference. The cardinality of fuzzy set  $X$  is defined as follows:

$$|X| = \sum_x \mu_X(x). \quad (7)$$

The cardinality of a crisp set is simply the number of its elements.

### 2.3. Gray-scale morphological operators and their properties

We define basic gray-scale morphological operators using fuzzy set concepts. We also list a number of their important properties. Throughout the paper we use only a flat structuring element that is described by a crisp subset and that acts as an image mask or a probing window. The erosion of fuzzy set  $X$  by the flat structuring element  $B$  is defined by analogy to the binary erosion

$$X \ominus B = \bigwedge_{b \in B} X_{-b}.$$

It can be shown that the eroded value at pixel  $x$  is a minimal value of the image intensity  $\mu_X$  in the window defined by the flat structuring element  $B$  when its origin is at  $x$ . The dilation of fuzzy set  $X$  by flat structuring element  $B$  is defined by analogy to the binary dilation

$$X \oplus B = \bigvee_{b \in B} X_b.$$

It can be shown that the dilated value at pixel  $x$  is a maximal value of the image intensity  $\mu_X$  in the window defined by flat structuring element  $B$  when its origin is at  $x$ .

Structural opening of the fuzzy set is defined by erosion followed by dilation, as in the binary case, Eq. (1). We now list the properties of the opening operator which are important to our further discussion. Structural opening is a translation invariant operator, that is,

$$X_z \circ B = (X \circ B)_z \quad (8)$$

and is anti-extensive, that is

$$X \circ B \preceq X. \quad (9)$$

Structural openings are increasing, i.e, they preserve the ordering relations between images:

$$X \preceq Y \Rightarrow X \circ B \preceq Y \circ B. \quad (10)$$

Structural openings are idempotent, i.e, the successive application of structural opening does not further modify the image:

$$(X \circ B) \circ B = X \circ B. \quad (11)$$

Transformations that are increasing, idempotent and anti-extensive satisfy the intuitive requirements for filters.

## 2.4. Algebraic opening, top-hat and rank filters

As we have seen, the anti-extensive, increasing and idempotent properties are inherent to structural opening. Generalized image transformations that satisfy these three properties are called algebraic openings, or simply openings. There are algebraic openings that cannot be implemented by erosion followed by dilation with the same structuring element, i.e., openings that are not structural. Area opening and opening by reconstruction are examples of such generalized openings [4]. We denote the opening operator by  $\gamma$ . To simplify equations, we sometimes omit the extra brackets when sequential openings are applied to some set  $X$ . We should remember that, in this case, the order of operator application is from right to left, i.e.,  $\gamma_3\gamma_2\gamma_1(X) = \gamma_3(\gamma_2(\gamma_1(X)))$ . Various types of openings are used to extract or filter image details with specific properties. In the following we introduce density opening, which takes into account the size, shape and density of grouped details (blob clusters).

The other transformation we will use is a top-hat transformation. This is simply the difference between the initial image and the opened one (which is always smaller because of the anti-extensive property). This transformation is denoted by  $\rho$  and is defined as

$$\rho(X) = X - \gamma(X).$$

The top-hat results in an image containing the details that would be removed by opening.

Erosion and dilation can be related to the so-called rank or order statistic filters. We denote this filter by  $R_{B,k}$ , where  $B$  is the filter window used and  $k$  is its rank. The filter window is centered at each image pixel  $x$  of image  $X$  and the output value of the rank filter at this point is obtained by ascending ordering of the intensities of pixels below the window and selection of the  $k$ th value. Rank  $k$  may vary from 1 to the number of elements in set  $B$  (cardinality of  $B$ ). It is clear that erosion and dilation can be obtained by rank filtering with rank equal to 1 and  $|B|$ , respectively, i.e.,  $X \ominus B = R_{B,1}(X)$ ,  $X \oplus B = R_{B,|B|}(X)$

### 3. Size distributions

#### 3.1. Granulometries

The concept of granulometry is related to the filtering or sieving of grain particles through some predefined structure. This concept is directly applicable to binary images and can be extended to gray-scale images. The sieving of image particles can be implemented by a structural opening operator  $B_r$  with SE of size  $r$ ; the SE acts as the sieve structure. By using a sequence of increasing SEs, we can obtain a sequence of filtered images. Each image within this sequence, called an opening or granulometric sequence, has grain content of size greater than the size of the SE used. Introduced by Matheron [13], abstract granulometry is mathematically defined by an opening transformation  $\gamma_r$  with parameter  $r$ , which must satisfy:

$$p \geq r \Rightarrow \gamma_p \preceq \gamma_r. \quad (12)$$

Equation (12) is equivalent to the following two inequalities for opening operators:

$$\gamma_p \gamma_r = \gamma_p \quad (13)$$

$$\gamma_r \gamma_p = \gamma_p. \quad (14)$$

The Eqs. (13) and (14) present the absorption property of the operator. It should be emphasized that Eqs. (12),(13) and (14) are equivalent in general only for the openings [22]. The openings that satisfy the absorption property, and therefore property (12), are suitable for building of granulometry. Granulometry built by structural opening is called structural granulometry. Restrictions should be applied to a family of structuring elements  $B_r$ , since not all families will satisfy the property (12). A family of SEs satisfying  $B_p = B_p \circ B_r$  for all  $p, r$ , such that  $p \geq r$ , is called a mutually open family, which fulfills the property (12), see [22]. It is necessary for a family of SEs (which build granulometric sequence) to be mutually open, see [22]. A family of SEs  $B_r$  generated from some single prototype  $B$  by its  $r$ -times sequential dilation  $B_r = \underbrace{B \oplus B \oplus \dots \oplus B}_{r \text{ times}} \equiv rB$

is commonly used in granulometry. Due to its construction, such a family is mutually open, and therefore is suitable for building granulometry. Each pattern  $rB$  is similarly shaped, with size controlled by the parameter  $r$ . We say that structuring element  $rB$  has (digital) size  $r$ . In the following we use the disk-like prototype  $B$  unless otherwise noted.

#### 3.2. Opening pattern spectrum

The detail images  $\lambda_r$  of an opening sequence are the images obtained by subtraction of successive images of an opening sequence  $\lambda_r = \gamma_r - \gamma_{r+1}$ . The pattern spectrum of a discrete image  $X$  is defined as

$$PS(r) = \frac{|\gamma_r(X) - \gamma_{r+1}(X)|}{|X|} = \frac{|\lambda_r(X)|}{|X|}. \quad (15)$$

When opening,  $\gamma_r$  is a structural opening with a discrete size parameter  $r$  it produces a histogram of the sizes of image blobs (in the form of SEs). Opening with zero discrete size means opening by a single pixel that does not change the image. Opening by SE with a discrete size one means opening by a unit prototype SE. Obviously, the pattern spectrum can be also rewritten in the following form:

$$PS(r) = \frac{|\gamma_r(X)| - |\gamma_{r+1}(X)|}{|X|}$$

For some large (relative to image content) value of  $r = m$ , opened image  $\gamma_m(X)$  will be an empty set. Therefore, the pattern spectrum values must sum to one:

$$\sum_{r \geq 0} PS(r) = \frac{|\gamma_0(X)| - |\gamma_m(X)|}{|X|} = 1.$$

Thus, the pattern spectrum can be referred to as a size distribution of image grains. Examples of pattern spectra are shown in Fig. 2. They correspond to the artificial binary images shown in Fig. 1.

### 3.3. Top-hat pattern spectrum

Detail images  $\lambda_r$  have no details large enough to include an  $(r+1)B$  pattern. However, pieces much smaller than  $rB$  can appear in detail images. In [2] the author suggests building size distributions using detail images of top-hat image sequences. Each detail image  $\tau_r$  within this sequence is opened by  $rB$  and has no details large enough to include an  $(r+1)B$  pattern. Therefore, images within the sequence  $\tau_r$  are band-limited in the sense that the size of their details is bounded between  $r$  and  $r+1$ . This property of  $\tau_r$  is desired for building true size distributions of image contents. The other advantage of a top-hat spectrum is that the absorption property of opening is not required. A top-hat pattern spectrum can be generated by a family of structuring elements with the only inclusion requirement  $rB \subset (r+1)B$ ; no mutually open family of SEs is required.

The detail image sequence of  $X$  is built by the following iterative algorithm:

$$\text{detail images:} \quad \tau_r = \rho_{r+1} \circ rB \quad (16)$$

$$\text{top-hat sequence:} \quad \rho_r = \rho_{r+1} - \tau_r, \quad (17)$$

when sequences are computed in descending order  $r = N, \dots, 0$ . The algorithm starts with  $\rho_{N+1} = X$ . Note that  $\rho_r$  is a sequence generated by a top-hat transformation. The  $\tau_r = \rho_{r+1} - \rho_r$  images are referred to as detail images of a top-hat sequence, analogous

to detail images  $\lambda_r$  of an opening sequence  $\gamma_r$ . Application of the cardinality measure to the detail image sequence  $\tau_r$  yields a top-hat pattern spectrum:

$$PS_B(r) = \frac{|\tau_r(X)|}{|X|}. \quad (18)$$

## 4. Density opening operator

### 4.1. Introduction of density opening

Structural opening of the fuzzy set is defined by Eq. (1). There is a simple geometric meaning of the opening of a gray-scale image, by analogy to the intuition behind the binary opening in Eq. (2), when the umbra concept is used [16]. However, from the fuzzy set point of view there is no such analogy. Here we define another opening operator with some relaxation on set inclusion. It is directly defined in terms of fuzzy set concepts (the Eq.(1) is not valid for it) and shares the intuitive meaning of Eq. (2). This operator is less sensitive to image noise and can be used in the detection of clusters of different tightness, as illustrated later.

We define an operator (applied to both binary and gray-scale images) that builds the output image as follows. Given structuring element  $B$  and density parameter  $d \in [0, 1]$ , the density below the structuring element is measured at all possible positions. If it is equal to or greater than  $d$ , a piece of the initial image below the SE is copied to the output image. We define the density concept below. For a binary image, we can write the operator applied to a crisp set  $X$  in the following mathematical form:

$$\begin{aligned} \theta_{B,d}(X) &= \bigcup_{x:D(B_x,X) \geq d} (B_x \cap X) \\ D(B_x, X) &= \frac{|B_x \cap X|}{|B_x|}, \end{aligned} \quad (19)$$

where  $D(B_x, X)$  represents the average value or density of  $X$  below the mask  $B_x$  and  $|\cdot|$  is the cardinality of the set. This operator can be termed opening, since it satisfies all three axioms for algebraic opening, as will be shown in the next. We call this operator a *density opening*. In the case of maximal density  $d = 1$ , it corresponds to a regular morphological opening operator:

$$\begin{aligned} \theta_{B,1}(X) &= \bigcup_{x:D(B_x, X) \geq 1} (B_x \cap X) = \bigcup_{x:|B_x \cap X|=|B|} (B_x \cap X) \\ &= \bigcup_{x:B_x \subseteq X} B_x = X \circ B. \end{aligned}$$

Note that if  $d \neq 1$ , the operator cannot be implemented by erosion followed by dilation, and therefore it is only an algebraic opening and not a structural opening. We can extend this operator to work with gray-scale images by means of fuzzy set concepts.

Given the crisp set  $B$  of structuring element and density parameter  $d \in [0, 1]$ , the density opening operator applied to a fuzzy set  $X$  is defined as follows:

$$\theta_{B, d}(X) = \bigvee_{x: D(B_x, X) \geq d} (B_x \wedge X) \quad (20)$$

$$D(B_x, X) = \frac{|B_x \wedge X|}{|B|} = \frac{\sum \mu_{B_x \wedge X}}{\sum \mu_B}, \quad (21)$$

where  $D(B_x, X)$  represents the average value or density of  $X$  below mask  $B_x$  and summation is performed over the whole reference set  $E$ . This operator is constructed to work with gray-tone images and can be called an opening, since it satisfies the three axioms for algebraic opening, as we show in the following subsection. The binary operator defined in Eq. (19) is a partial case of the gray-scale operator in Eq. (20). The density opening operator does not coincide with structural opening operators for any value  $d$ . On the other hand it shares the main idea of the geometric meaning of the binary opening defined by Eq. (2). That is we can consider the density opening as the union of the parts of the original image that partially match the structuring element (as compared to the traditional opening, where the matching must be complete).

## 4.2. Operator properties

In this section we show the properties of the density opening operator that allow it to be effectively used in image analysis applications. We denote the set  $\{x \mid D(B_x, X) \geq d\}$  by  $T(X, B, d)$ . To simplify notation, we sometimes write  $T_d$  instead of  $T(X, B, d)$ .

**Proposition 1** *The density opening is anti-extensive*

$$\theta_{B, d}(X) \preceq X.$$

Since the output image is built from patches of the initial image, it is clear that the output image is ‘smaller’ than the argument image and therefore the density operator is anti-extensive.

**Proof.**

$$\theta_{B, d}(X) = \bigvee_{x \subseteq T_d} (B_x \wedge X) = (\bigvee_{x \subseteq T_d} B_x) \wedge X \preceq X,$$

where we have used Eqs. (4) and (5).

**End of proof.**

**Proposition 2** *The density opening is increasing:*

$$X \preceq Y \Rightarrow \theta_{B, d}(X) \preceq \theta_{B, d}(Y).$$

During construction of the output image, we measure the density of argument image below the SE. If the patch of  $X$  below  $B_x$  has a sufficient density, it is copied to the output image  $\theta_{B,d}(X)$ . At the same position  $x$ , image  $Y$  will also have sufficient density (since  $Y$  is ‘greater’ than  $X$ ). Therefore, the appropriate image patch of  $Y$  will be copied to  $\theta_{B,d}(Y)$ . Thus, it is guaranteed that  $\theta_{B,d}(X) \preceq \theta_{B,d}(Y)$ . This is rigorously proved in Appendix A1..

**Proposition 3** *The density opening is idempotent*

$$Y = \theta_{B,d}(X) \Rightarrow Z = \theta_{B,d}(Y) = Y. \quad (22)$$

The opened image  $Y$  is composed of the initial image masked by the SEs centered at positions  $x$  from set  $T(X, B, d)$ . At these positions  $x$ , the density measure of  $Y$  below  $B_x$  will be greater or equal to  $d$ . Therefore, the image  $Z$  obtained after repeated opening should contain image  $Y$ , that is,  $Z \succeq Y$ . However, since density opening is anti-extensive ( $Z \preceq Y$ ), it follows that  $Z = Y$  and therefore Eq. (22) will hold. This is rigorously proved in Appendix A2..

**Proposition 4** *The density opening is an algebraic opening.*

This is due to the anti-extensivity, increasing and idempotent properties of density opening.

**Proposition 5** *Density opening is translation-invariant.*

**Proposition 6** *The binary density opening operator defined in Eq.(19) is equivalent to the rank-max opening <sup>2</sup>.*

**Proof.**

The Rank-max opening operator is defined as follows:

$$RM_{B,k}(X) = (R_{B,k}(X) \oplus B) \wedge X \quad (23)$$

Using Eq. (5) and the notation of rank filters we can write

$$\begin{aligned} \theta_{B,d}(X) &= \bigcup_{x:D(B_x,X) \geq d} (B_x \cap X) = \bigcup_{x:R_{B,k}(x)=1} (B_x \cap X) = \left( \bigcup_{x \in R_{B,k}(X)} B_x \right) \cap X \\ &= \{R_{B,k}(X) \oplus B\} \cap X = RM_{B,k}(X) \end{aligned}$$

where

$$k = |B| - d * |B| + 1 = |B| * (1 - d) + 1 \quad (24)$$

is a rank of the rank filter  $R$  and  $B$  is a filter window. Here  $y = R(x)$  means that  $y$  is an output of the spatial rank filter at point  $x$ , but  $Y = R(X)$  means that a filter applied to the whole binary image (set)  $X$  yields an output set  $Y = \{y \mid R(y) = 1\}$ .

**End of proof.**

---

<sup>2</sup>Rank-max opening operator was described in [3, 4, 11]

**Proposition 7** *The absorption property of density opening is not satisfied with respect to the SE size parameter.*

This can be proven from a simple example.

**Proof.**

Suppose that we have a gray-tone image of a disk with density increasing from the center to the border, as on the left of Fig. 3. Application of a density opening operator, with  $r$  equal to the disk radius and  $d$  slightly smaller than the density of the whole disk, would not change the disk object. On the other hand, application of density opening with some smaller radius, and same density parameter  $d$ , will remove the center of the object. This is illustrated in Fig. 3. The example shows that the inequality

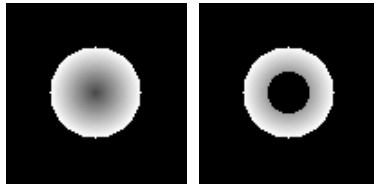


Figure 3: Left: Original image. Opening, with size parameter equal to the radius of the whole disk object ( $r = 25$ ), and 'd' slightly smaller than the density of the disk object  $d = 0.7$ , do not change the initial image. Right: opening with smaller size parameter  $r = 3$  and same  $d = 0.7$ .

$$r_1 > r_2 \Rightarrow \theta_{r_1}(X) \preceq \theta_{r_2}(X)$$

is **not** satisfied in general, and therefore the absorption property does not hold.

**End of Proof.**

**Proposition 8** *The absorption property of the density opening is satisfied, with respect to the density parameter*

$$d_1 > d_2 \Rightarrow \theta_{d_1}\theta_{d_2}(X) = \theta_{d_2}\theta_{d_1}(X) = \theta_{d_1}(X) \quad (25)$$

Before we prove this property, we justify it by simple considerations.

Given  $d_1 > d_2$ , during formation of the opened images  $\theta_{d_1}(X)$  and  $\theta_{d_2}(X)$ , the density below a moving SE is measured. When the density measured is greater than  $d_1$ , it is also greater than  $d_2$ . Therefore, all patches that form  $\theta_{d_1}(X)$  are included in  $\theta_{d_2}(X)$ . In this way,  $\theta_{d_2}(X)$  must contain  $\theta_{d_1}(X)$  implying

$$\theta_{d_1}(X) \preceq \theta_{d_2}(X). \quad (26)$$

Earlier (in sec. 3.1), we showed that an algebraic opening that satisfies Eq. (26) for any  $d_1 > d_2$ , must also satisfy the absorption property in Eq. (25). Now we rigorously prove, that the family of density opening operators with different values of  $d$  satisfy Eq. (26) for  $d_1 > d_2$  and the absorption property in Eq. (25).

**Proof.**

Given  $d_1 > d_2$ , this means that

$$T_{d_1} = \left\{ x \mid \frac{\sum \mu_{B_x \wedge X}}{\sum \mu_B} \geq d_1 \right\} \subseteq \left\{ x \mid \frac{\sum \mu_{B_x \wedge X}}{\sum \mu_B} \geq d_2 \right\} = T_{d_2},$$

$$\theta_{d_1}(X) = \bigvee_{x \in T_{d_1}} (B_x \wedge X) \preceq \bigvee_{x \in T_{d_2}} (B_x \wedge X) = \theta_{d_2}(X),$$

where the last inequality follows from the set inclusions  $T_{d_1} \subseteq T_{d_2}$  just shown and the inequality in Eq. (3). Finally, from the proven inequality (26) and the three properties of algebraic opening, it follows that the density opening satisfies the absorption property (25).

**End of Proof.**

Due to the absorption property, a density opening with a constant size parameter and increasing density generates a granulometric  $\theta_{d(n)}$  image sequence, where  $d(n)$  denotes the  $n$ -th increasing density parameter of the density opening. Detail images  $\lambda_{d(n)} = \theta_{d(n)} - \theta_{d(n+1)}$  decompose the initial image  $X$

$$X = \theta_1 \vee \bigvee_{d=\{0,1\}} \lambda_d, \quad (27)$$

when they are disjoint, i.e.,  $\forall d_1, d_2 \in [0, 1], \lambda_{d_1} \vee \lambda_{d_2} = \emptyset$  holds. Note that the decomposition in Eq. (27) is applied to both binary and gray-tone images. Each detail image has its own inherent density of apparent structures. Detail images can be further used for building the pattern density spectrum for cluster analysis, as shown in Section 5.2.

Now we illustrate the differences between density opening, structural opening and rank-max opening as applied to binary and gray-tone images. As was shown, the binary version of density opening coincides with rank-max opening. Application of these operators to the binary image in Fig. 4(a) is shown in Fig. 4(c). The parameters  $r, d$  were set to the size and density of the disk object (cluster of small blobs). The image filtered by structural opening is shown in Fig 4(b). The parameter  $r$  was set to the size of blobs that constitute the object. The same result would be obtained for density opening with  $d = 1$  and  $r$  equal to the blob size. In contrast to structural opening, density opening is capable of extracting the whole clustered object. It should be noted that the size parameter for density opening should not be set exactly to the size of the cluster, since the cluster can be composed of smaller structuring elements with similar density parameters. This is illustrated in Fig. 4(d). Appropriate selection of the density and size parameters will allow the extraction of separable blobs as well, even from a noisy background. Application of the density operator to gray-tone images is shown in the following examples. The structural opening of the initial image Fig. 5(a) is shown in Fig. 5(b). The size parameter was set to the radius of the blobs ( $r = 3$ ) that make up the object. Density opening with the same size parameter is shown in Fig. 6(a). In contrast to the binary case, density opening does not coincide with structural opening for any values of  $d$ . Setting the density parameter to one would

yield a black image (empty set). Density openings with size parameter  $r$  equal to the cluster radius and half of the cluster radius are shown in Fig. 6(b,c). The  $d$  parameter was set to match the density of the object. There is also no coincidence of density opening with rank-max opening, as occurs in the binary case. Rank-max openings are shown in Fig. 7 for a number of size and rank parameters. They differ conceptually from density opening and result in largely varying output images.

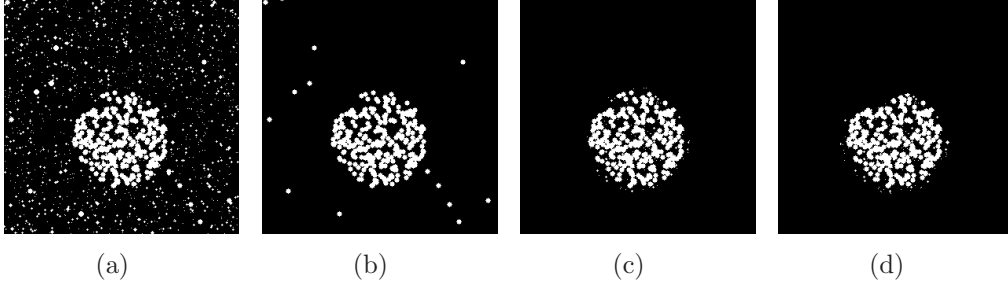


Figure 4: Filtering of the binary images by structural and density openings. The approximate size and density of the cluster are  $R = 60, D = 0.5$ , respectively. (a) Initial binary image. (b) Structural opening ( $r=3$ ). The density opening with 'd=1' yields the same result. (c) Density opening ( $r=60, d=0.5$ ). (d) Density opening ( $r=30, d=0.5$ ).

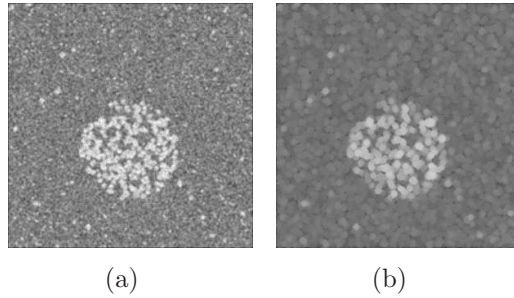


Figure 5: Filtering of a gray scale image by structural opening. (a) Initial gray scale image. The approximate size and density of the cluster are  $R = 60, D = 0.67$  (b) Structural opening ( $r=3$ ).

## 5. Use of density opening to quantify size and density information in image scenes

### 5.1. Pattern size spectrum

In this section we introduce a *pattern size spectrum* built by density opening  $\theta_r$  with constant density and varying size parameter  $r$ . Opening  $\theta_r$  does not satisfy the absorption property and therefore a valid granulometric sequence cannot be obtained. However, it is still possible to form a top-hat sequence as in Eq. (16) and a corresponding pattern spectrum as in Eq. (18). Such a pattern spectrum will be useful for estimating not only the size distribution of image particles or blobs, but also of the

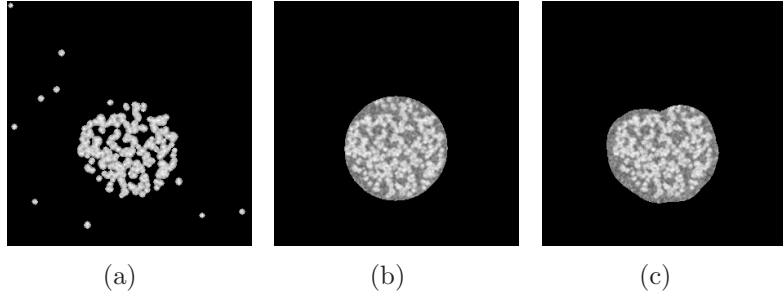


Figure 6: Filtering of a gray scale image by density openings. The initial gray scale image is shown in Fig 5(a). (a) Density opening ( $r=3, d=0.75$ ). (b) Density opening ( $r=60, d=0.67$ ). (c) Density opening ( $r=30, d=0.67$ )

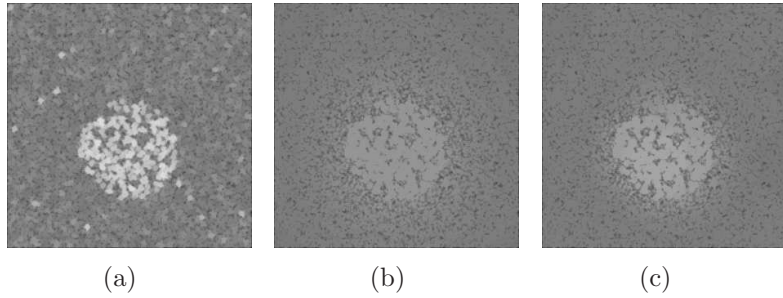


Figure 7: Rank-Max filtering of the gray scale images. The initial gray scale image is shown in Fig 5(a). (a) rank= $k(d=0.75), r=3$ . (b) rank= $k(d=0.67), r=60$ . (c) rank= $k(d=0.67), r=30$ . Where  $k()$  is defined in (24)

sizes of blob clusters in the image. Given a constant density  $d$  and some prototype structural element  $B$ , we apply the algorithm (16)–(18) using density opening  $\theta_r$  with constant  $d$  in place of structural opening:

$$\tau_r = \theta_r(\rho_{r+1}), \quad (28)$$

$$\rho_r = \rho_{r+1} - \tau_r, \quad (29)$$

$$PS_d(r) = \frac{|\tau_r(X)|}{|X|}, \quad (30)$$

with sequences computed in decreasing order  $r = N, \dots, 0$  and where the algorithm starts with  $\rho_{N+1} = X$ . Here,  $r$  is used for ordering the iterative process and for denoting the SE digital sizes. The pattern spectrum  $PS_d(r)$  generated is a size distribution of apparent image clusters with density  $d$ . Examples of top-hat pattern spectra generated by density opening are presented in Fig. 8. The initial image in Fig. 8(a) is a gray-tone image that contains evident tight clusters. Fig. 8(b) shows the pattern spectrum with  $d$  approximately equal to the density of clusters in the image analyzed in Fig. 8(a). There are three, clearly distinguished, large spikes corresponding to the three clusters in the initial gray-tone image. The location of these spikes quantifies the sizes of image clusters. Fig. 8(c) shows an opening spectrum with high  $d$ . From this pattern size spectrum, the average size of blobs that form image clusters can be

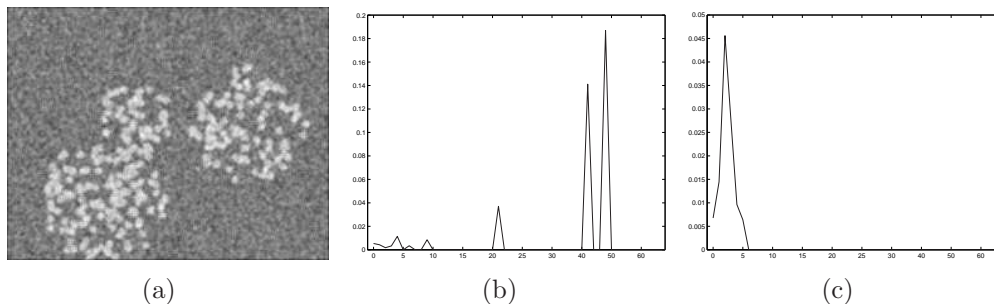


Figure 8: Pattern Size Spectrum by density opening. (a) Initial gray tone image. (b) Pattern size spectrum with  $d$  ( $d = 0.61$ ) close to the density of the clustered objects. (c) Pattern size spectrum with high  $d$  ( $d = 0.8$ ).

estimated. Using  $d$  slightly less than one yields a more stable estimation of blob sizes in a noisy environment. Note that for the curves shown in Fig. 8(b) and 8(c), the summations  $\sum_{r \geq 0} PS_d(r)$  are not equal to one. This occurs for gray-tone images when their background area has a density lower than a constant density  $d$  of the density opening operator  $\theta_r$  used. The operator  $\theta_r$  will not open parts of the background area, even with zero-size SEs ( $r = 0$ , a single dot). The background remains in the last image  $\rho_0$  of the top-hat sequence.

Thus, the pattern size spectra in Fig. 8(b) and 8(c) ignore the background information of the gray-tone image in Fig. 8(a). Therefore, the pattern size spectrum of gray-tone images should be normalized when it is used as a size distribution.

## 5.2. Pattern density spectrum

Density opening satisfies the absorption property (25) with respect to the density parameter  $d$ . Therefore, an operator  $\theta_d$  is suitable for the generation of a granulometric image sequence, which can then be used for the development of a *pattern density spectrum*:

$$PS_r(d) = \frac{|\theta_{d(n)}(X) - \theta_{d(n+1)}(X)|}{|X|}, \quad (31)$$

where  $d(n)$  denotes the  $n$ -th increasing density parameter of the density opening,  $n \in [1, N]$ ;  $d(1) = 0$ ;  $d(N) = 1$ . The pattern density spectrum can be viewed as a distribution of blob densities in the image analyzed<sup>3</sup>. Examples of density spectra for binary images are shown in Fig. 9. Density spectra can be used for cluster detection and estimation of their densities. The density coordinates of the two peaks in Fig. 9(b) and 9(c) correspond to the real densities of clusters in Fig. 9(a). For estimation

<sup>3</sup>When an image contains crisp subsets (tight blobs), which can include the SE used, the summation  $\sum_{d=0, \dots, 1} PS_r(d)$  is smaller than one. The crisp subsets will remain in the last opened image  $\theta_1(X)$  of the granulometric sequence. In this case, the area of  $|\theta_1(X)|$  should be assigned to the last additional  $N + 1$  value of the pattern spectrum to obtain a valid distribution function  $PS_r(d)$ .

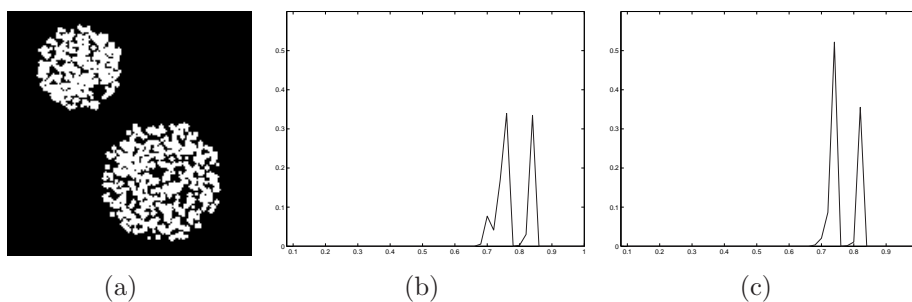


Figure 9: Density Spectra. (a) Initial binary image. (b) Density Spectrum. Density opening operator has size parameter  $r = 40$ , smaller than the size of the smaller blob cluster, equal to 50. (c) Density Spectrum. The density opening operator has size parameter  $r = 50$ , i.e. equal to the size of the smaller blob cluster.

of cluster densities, the constant size parameter  $r$  should be selected smaller than the minimal cluster size and much greater than the size of the blobs that constitute the clusters. If there are clusters smaller than the value  $r$  selected for density opening, the estimated densities would be smaller than the actual values. These smaller densities are average values of the density of clusters and the adjacent background below the larger SE.

The density spectrum of a gray-tone images is usually more complex. An example of a density spectrum of gray-tone image with a noisy background is shown in Fig. 10(b). The initial gray-tone image in Fig. 10(a) is a binary image corrupted by additive noise and smoothed by a low-pass filter with a small square window. The two right-hand

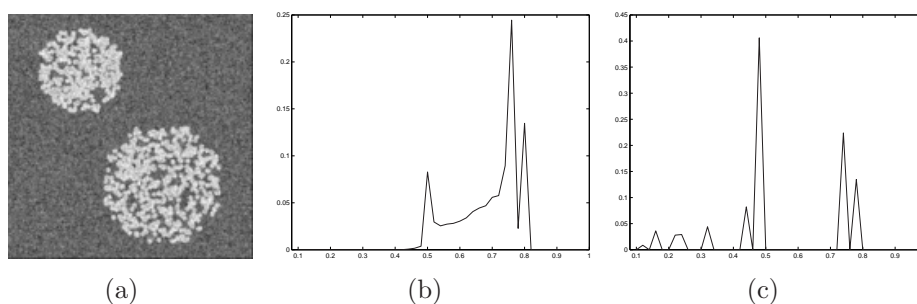


Figure 10: Density Spectra. (a) Initial gray tone image. (b) Density Spectrum. Density opening operator has size parameter  $r = 50$ , equal to the size of the smaller blob cluster. (c) Density Spectrum generated by top-hat transform. The size parameter is equal to the size of the smaller blob cluster ( $r = 50$ )

spikes in the density spectrum in Fig. 10(b) correspond to the observed clusters; the third spike, on the left, corresponds to the background. The intermediate part between the left and the middle peak also corresponds to the background area removed during sequential opening.

The density spectrum can also be generated by top-hat transformation. Given a prototype structural element  $B$  of size  $r$ , we apply the algorithm of Eqs. (16)–(18) using density opening  $\theta_d$  with constant  $r$  in place of structural opening:

$$\tau_d(n) = \theta_d(n)(\rho_d(n+1)), \quad (32)$$

$$\rho_d(n) = \rho_d(n+1) - \tau_d(n), \quad (33)$$

$$PS_r(d) = \frac{|\tau_d(X)|}{|X|}, \quad (34)$$

with sequences computed in decreasing order  $n = N, \dots, 1$  and  $d(n)$  is a sequence of decreasing densities, such that  $d(N) = 1$ ,  $d(1) = d_{min}$ . The algorithm starts with  $\rho_{d(N+1)} = X$ . If  $d_{min} = 0$  the summation  $\sum_{d=0, \dots, 1} PS_r(d)$  is necessarily equal to one, and the last image  $\rho_0$  within the descending top-hat sequence is an empty set. Therefore, the pattern spectrum  $PS_r(d)$  generated can be regarded as a density distribution of clusters apparent within the image. If  $d_{min}$  is greater than zero, the image parts with densities lower than  $d_{min}$  (for example, the background) are not quantified by the density spectrum in Eq. (34). In this case, the density spectrum should be normalized to be a valid size distribution function. An example of a top-hat pattern density spectrum of the gray-tone image in Fig. 10(a) is illustrated in Fig. 10(c). It was generated by density opening with constant  $r$  equal to the size of the smaller cluster in the image scene. The top-hat density spectrum in Fig. 10(c) differs from the opening density spectrum in Fig. 10(b), but they both have similar features. Two right-hand spikes, corresponding to clusters in the image scene, and the left-hand spike, corresponding to the background, show the same densities along the horizontal axis. Therefore, density spectra generated by opening or top-hat transformation can be used for quantification of density information within an image.

### 5.3. Size–density signatures

The pattern size spectrum  $PS_d(r)$  quantifies the size distribution of tight constellations. It requires the knowledge of approximate densities of clusters expected to appear within an image. Often, we have no such knowledge. It is possible, however, to compose a 2D *size-density spectrum* from a group of pattern size spectra computed for a set of densities. Thus, the image information is converted to a 2D size–density map. Fig. 11(a) shows an example of a size–density spectrum for the binary image in Fig. 9(a). The horizontal axis is calibrated in size units and the vertical axis in density units. The dimensions of the spectrum depend on the requirements for discrete steps in density and size coordinates.

There are other possibilities for forming 2D spectra for further extraction of size–density information about blob arrangement in an image. Alternatively, we can build density spectra  $PS_r(d)$  for a sequence of desired constant size parameters for the density opening. Composition of pattern density spectra will result in another type of 2D size–density spectrum. The pattern density spectrum can be obtained in two ways, using an opening image sequence or a top-hat image sequence, and therefore we can form two additional variants of size–density spectra. Fig. 11(b) and 11(c) show examples of these variants of size–density spectra for the binary image in Fig. 9(a). Size–density spectra are characterized by specific signature drawings when an image contains evident blob clusters. For this reason, we call these 2D maps *size–density signatures*. In what follows, we call a signature generated by composition of a top-hat size spectra a type 1 signature; a type 2 signature is generated by composition of density opening spectra; and a type 3 signature is generated by composition of top-hat

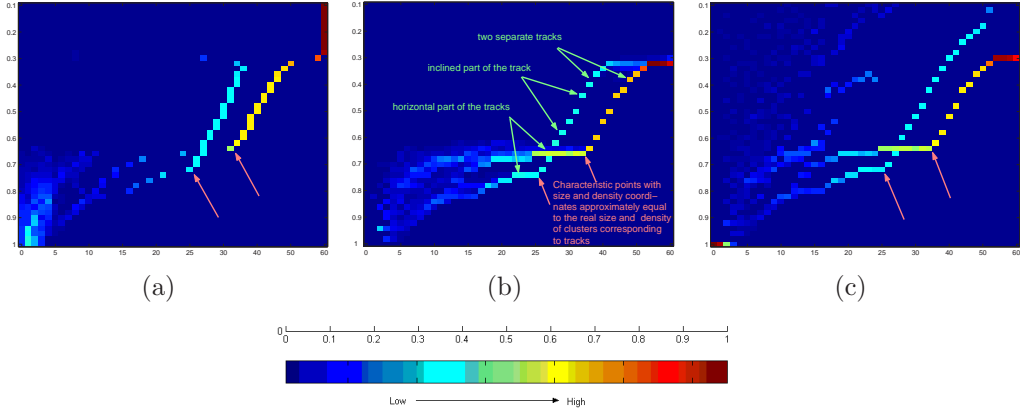


Figure 11: Size-density signatures of binary image 9(a). Red arrows point to the regions with density and size coordinates equal to the size and density properties of clusters on the analyzed image 9(a). (a) Signature map built by composition of size top-hat spectra (type 1 signature). (b) Signature built by composition of density opening spectra (type 2 signature). (c) Signature built by composition of density top-hat spectrums (type 3 signature).

density spectra. Although the three types of size–density signatures differ from each other, they have common features useful for quantifying size–density aspects of image blob arrangements. Looking at the size–density signatures of Fig. 11, we can see two separate tracks. The tracks start from low size and high densities and continue to large size and low densities. Each track corresponds to an individual cluster from the binary image in Fig. 9(a). We can recognize two distinct parts on the tracks in Fig. 11(b) and 11(c): horizontal and inclined segments. The horizontal part of the tracks indicates similar stable densities, which appear in 1D density spectra when the SE size is restricted to some interval. The inclined part indicates a reduction in density when SE increases beyond this specific interval. Fig. 12 explains the track behavior. While the SE size is equal to or somewhat smaller than the real size of the cluster analyzed ( $r = r_1, r_2$ ), the peak in  $PS_r(d)$  is positioned at the same density coordinates ( $d_1 = d_2$ ). This density is the real density of the cluster analyzed ( $D = d_1 = d_2$ ). When the SE size becomes greater than the size of the cluster analyzed ( $r_4 > r_3 > R$ ), the density measured ( $d_4, d_3$ ) under the SE will drop below the real cluster density  $D$ . The larger the SE, the smaller is the density measured. The rate of density reduction is inversely proportional to the square of increasing size:  $D_{measured}(r) \simeq \frac{D}{(r/R)^2}$ ,  $r > R$ . This relation approximately holds only when there is no noise around a tight cluster. The type 1 size–density signature in Fig. 11a has no horizontal part of the track. The 1D pattern size spectrum, with  $d$  set to the density of clustered data  $D$ , yields only a single peak (no track) corresponding to the real size of the cluster. The inclined part of the tracks is similar for all three signature types due to same reason, as illustrated by Fig. 12. In general, accurate inclined tracks with density reduction rates not much smaller than  $\frac{1}{r^2}$  indicate the appearance of clusters in an image. Their initial points with smallest size and highest density are marked by red arrows on the size density signatures in Fig. 11(a), 11(b) and 11(c). The marked regions have size and density coordinates matched to the real density and size of the clusters in the image. Additional information about individual blobs can be extracted from regions of low size and

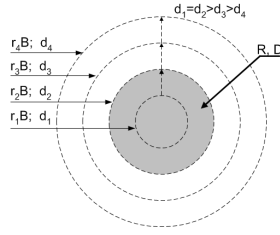


Figure 12: Density uncertainty of the analyzed object. The dense object of size  $R$  and density  $D$  is analyzed by structuring element with enlarging size  $r_{1..4}$ ,  $r_2 = R$ . The measured densities are  $d_{1..4}$ . The  $d_1$  and  $d_2$  are equal to the real density  $D$  of object, whereas  $d_{3..4}$  are the diminished densities.

high density in the signature images.

Examples of all three types of size–density signature for the gray-tone image in Fig. 10(a) are shown in Fig. 13. We can see similar tracks corresponding to tight clusters.

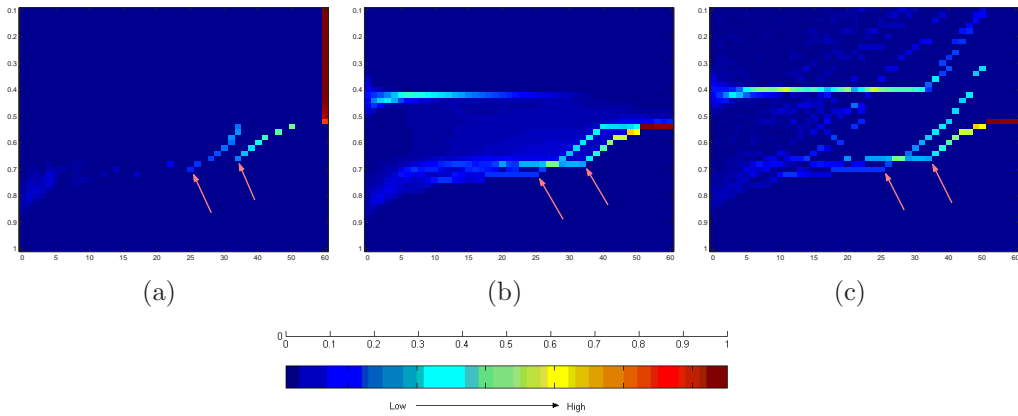


Figure 13: Size-density signatures of gray tone image 10(a). Arrows point to the regions with density and size coordinates equal to the size and density properties of clusters on the analyzed image 10(a). (a) Signature map built by composition of size top-hat spectra. (b) Signature built by composition of density opening spectra. (c) Signature built by composition of density top-hat spectra.

The rate of density reduction of the inclined part of the track is smaller due to the background intensity. In addition, in Fig. 13(b) and 13(c), we can see an accurate track with a long horizontal part at low densities. This corresponds to the background in the gray-tone image. The density of the background is identified by the density coordinate of the horizontal track. The horizontal track ends at some large size coordinate, which indicates the maximal size of the background segment entirely covered by the SE pattern used. There is no such background horizontal track on the type 1 size–density signature in Fig. 13(a). During calculation of 1D top-hat pattern size spectra for low densities (relative to the background), the entire image is opened on the first iteration of Eq. (32). This results in a vertical line at the maximum size coordinate of the signature in Fig. 13(a). Therefore, a size–density signature of type 1 disregards the background information.

It should be noted that size–density signatures depend only on the relative arrangement of blobs, and not on their actual positions in the image. This property is very useful for various pattern recognition tasks. At the end of this section we illustrate

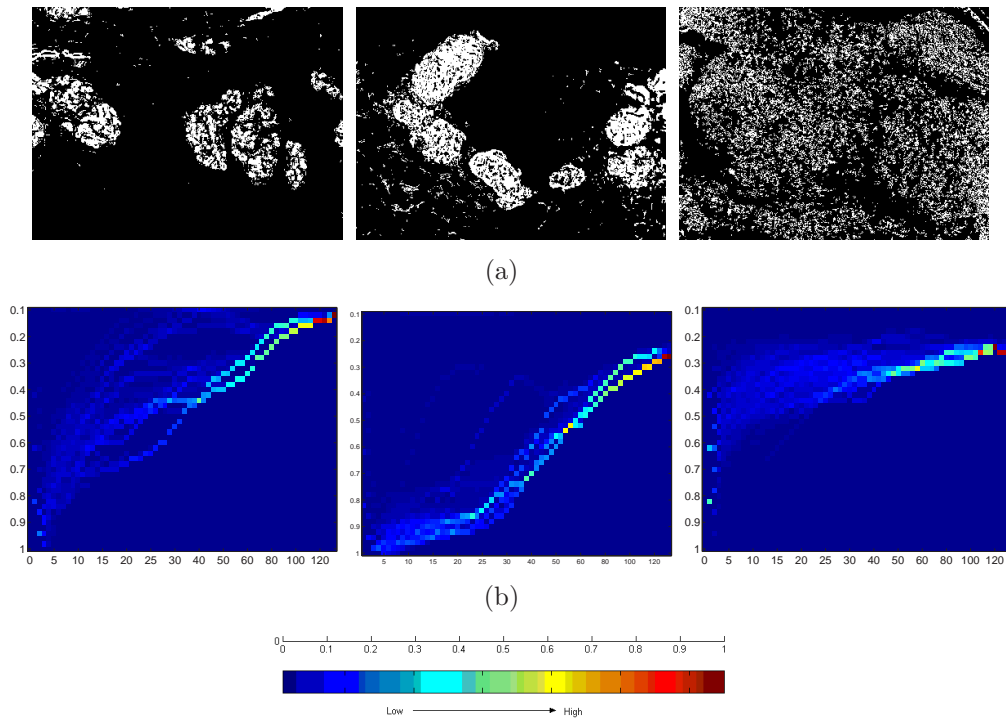


Figure 14: (a) Segmented microscopic images. (b) Corresponding size density signatures of type 2.

a number of signatures of real images. The size–density signatures are shown in Fig. 14(b). They correspond to the segmented biopsy microscopic images in Fig. 14(a), used in the diagnosis of breast cancer. Visually, we are still able to associate each spectrum to binary images by rough detection of density reduction tracks and the localization of their special features, described earlier for artificial images. The left signature possesses two well distinguished density reduction tracks which break out at  $(d \approx 0.45, r \approx 40)$  and  $(d \approx 0.6, r \approx 28)$ . The middle signature density tracks break out at much larger densities  $(d \approx 0.9)$  which correspond to the very tight clusters seen in the original image. The right signature has tracks of a very slow density reduction rate. This behavior corresponds to the absence of well formed distinct clusters. The tracks are located at regions of low densities  $(d \approx 0.35)$  which correspond to sparse image content. In the next section we discuss the automatic discrimination of images on the basis of size–density signatures.

## 6. Image discrimination by means of size-density signatures

Size–density signatures can be used to characterize and discriminate between different types of images. Visual inspection of image signatures allows differentiation between images that contain regions of clustered blobs of different sizes and densities (examples are shown in Fig. 1 and 15). For the automatic classification of images, further processing of size–density signatures is required. One possible approach is to use a

variant of the Hough transform to detect inclined tracks on image signatures. Extracted track parameters such as angle, coordinates of the end points and others can serve as features for final classification. We, however, suggest using of a different approach. The size–density signatures are directly supplied (simple feature selection is still performed, as described later) to a powerful classifier. As an example, we show that image signatures can be efficiently discriminated by the Support Sector Machine (SVM) technique [18, 19]. The signatures are first reshaped to vectors and then are supplied as inputs to SVM. It is desirable that these vectors will be insensitive to various transformations such as translation and rotation of image objects. The size–density signatures indeed achieve this goal. Each entry in the signature corresponds to some size–density information within the image and does not depend on translation or other transformations that do not change the size–density relations of clustered blobs. The size–density signatures have acceptable dimensions, in contrast to the initial image, for direct classification by SVM.

## 6.1. Artificial dataset

To check the capabilities of SVM classification techniques in conjunction with size–density signatures, we built an artificial database that contains three classes of binary  $256 \times 200$  images. We denote these cases as N, S, and I cases. All three types of images are formed by the composition of clustered small disks. The clusters are themselves built in circular form of large size. The regions occupied by clusters are randomly positioned and may overlap. The artificial images are characterized by the number of possible clusters, their sizes and their densities. Table 1 summarizes the selected parameters for each of the image cases. Some parameters in the table are represented by

|                   | N       | S       | I         |
|-------------------|---------|---------|-----------|
| Density           | 0.4     | 0.6     | 0.4       |
| Cluster size      | [30,60] | [30,60] | [100,130] |
| Number of objects | [2,3]   | [2,3]   | [1,2]     |
| Blob size         | 3       | 3       | 3         |

Table 1: Selected parameters of artificially generated images

intervals. This means that a parameter is selected randomly with uniform probability in the underlined interval. A number of examples of the images generated are shown in Fig. 15. The SVM was trained on a set of 450 images, 150 of each class. The testing was performed on 300 separate images, 100 from each class. Since the signatures are highly redundant (i.e., a major part of the signature consists of zero values), entries with zero values over the whole data set have been excluded. This procedure can be considered as the feature extraction stage. The simulations showed that classification of artificial patterns with the parameters listed in Table 1 achieve **zero errors** ( on the test set) for all three types of signature used. Thus, using image signatures in conjunction with SVM classification is very fruitful. Additional tests were performed on artificial data sets generated with parameters other than those indicated in Table 1. The largest error was equal to 0.6% when we used type 2 signatures. Additional

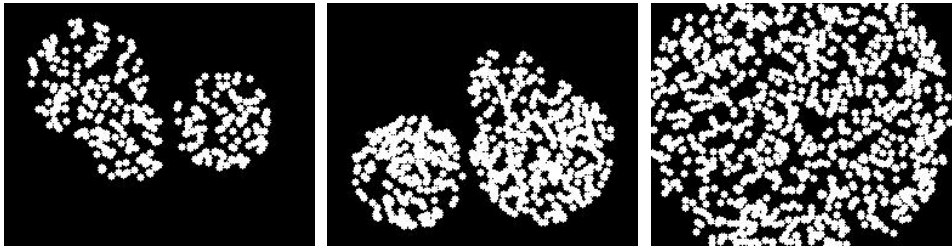


Figure 15: Three different cases of images from an artificially generated database.

classification tests on artificial and real data images [such as those shown in Fig. 14(a)] have shown that the most suitable signatures for automatic discrimination purposes are type 1 size–density signatures. The reason for this may lie in the highest redundancy of this type of signature. For additional details of this experiment see appendix B3..

## 6.2. Classification of histological images of breast tissue by means of size-density signatures

In this section we demonstrate the application of size-density signatures to the classification of real world medical images. The microscopic images of normal and cancerous breast tissue were obtained from the department of pathology of RamBam Medical Center in Haifa. They were manually labelled by an experienced pathologist into three classes corresponding to normal, invasive carcinoma and carcinoma in-situ cases. The labels were used for training and testing of an automatic classification system. The image database collected, contains 119 images of normal tissue, 102 images of carcinoma in-situ and 140 cases of invasive carcinoma. The images were acquired from paraffin embedded tissue sections that are mounted on transparent glass slides. The tissue sections were previously stained by commonly used Haematoxylin and Eosin (H&O) dyes to reveal different biological structures. The acquisition process was carried with use of Digital Nikon Coolpix 995 camera mounted on a Nikon Eclipse E600 microscope. The microscope magnification was set to x40. Such low magnification makes it possible to reveal architectural features of the tissue but not individual cellular features which are also taken into consideration in the manual diagnosis by experienced specialists. The images were cropped to  $385 \times 285$  pixels. The tissue nuclear structures, stained by H&O, appeared in shades of blue, while the stained cytoplasm and connective tissue appeared in shades of pink. To separate the cellular structures (it is assumed that cellular structures carry the main information for differentiating the cancerous tissue) we used a segmentation technique proposed in [22]. This technique is not intended for fine segmentation but is sufficiently robust to cope with variations in the staining and acquisition processes. Examples of segmented images are presented in Fig. 14(a). The segmented images were processed to obtain their size-density signatures of type 1. The signatures were reshaped to  $1D$  vectors and supplied to a SVM classifier. As in the case of the artificial images, entries with zero values over the whole data set have been excluded. Using a careful cross-validation testing setup, we achieve the correct diagnosis (coinciding with the pathologist decisions) in 92% of the cases for the 3-class

image database (note that a random guess would yield 33% success in this case). Some additional details on this experiment can be found in appendix B3., and an exhaustive description is given in [22].

## 7. Summary

In this paper we have developed a two-parameter operator that satisfies the requirements of algebraic opening. The operator can be applied to both gray-tone and binary images. The binary version of the operator coincides with rank-max opening [3, 4, 11]. We suggest the use of the proposed density opening operator for building of 2D extension of the morphological pattern spectrum. We refer to this approach as a pattern size–density spectrum, since it quantifies size–density aspects of image blob arrangements. In contrast to a regular pattern spectrum, the size–density spectrum takes into consideration spatial relations between image blobs. We have shown, using both artificial and real world medical images, that a size–density spectrum, in conjunction with the popular SVM classifier [18, 19] can be successfully used for discrimination between images that contain blob clusters of various sizes and densities. The proposed method works effectively with various types of images that can be described in terms of the size and density of blob constellations (biological medical, geological, and cosmological images).

The proposed density opening uses the flat structuring element. However, it can be extended to work with non flat structuring elements. In this case the weighted average is measured under a mask in place of the average (or density) defined in Eq. (21). It can be shown that this operator is an abstract opening, as well. Furthermore, it satisfies the absorption property with respect to a density parameter and therefore the size–density spectrum can be constructed on their basis. These issues, however, are beyond the scope of this paper and will be postponed to future work.

## 8. Appendix

### A Proofs for Section 4.

#### A1.

We denote the set  $\{x \mid D(B_x, X) \geq d\}$  by  $T(X, B, d)$ , where  $D(B_x, X)$  is the average density of  $X$  below a structuring element  $B_x$  defined in Eq. (21). We prove that the increasing property holds for the density opening operator. Given  $X \preceq Y$ , we want to show that  $\theta_{B,d}(X) \preceq \theta_{B,d}(Y)$ .

$$X \preceq Y \Rightarrow \forall x \quad \text{if } D(B_x, X) \geq d \quad \text{then } D(B_x, Y) \geq d$$

implying that  $T(X, B, d) \subseteq T(Y, B, d)$ . Thus,

$$\begin{aligned}\theta_{B,d}(X) &= \bigvee_{x \subseteq T(X,B,d)} (B_x \wedge X) \preceq \bigvee_{x \subseteq T(Y,B,d)} (B_x \wedge X) \preceq \bigvee_{x \subseteq T(Y,B,d)} (B_x \wedge Y) \\ &= \theta_{B,d}(Y)\end{aligned}$$

implying that  $\theta_{B,d}(X) \preceq \theta_{B,d}(Y)$ .

## A2.

Here we prove that density opening is idempotent:

$$\underline{Y = \theta_{B,d}(X) \Rightarrow Z = \theta_{B,d}(Y) = Y}$$

We denote the set  $\{x \mid D(B_x, X) \geq d\}$  by  $T_X$ , where  $D(B_x, X)$  is the average density of  $X$  below structuring element  $B_x$  defined in Eq. (21).

$$\begin{aligned}T_X &\equiv \{x \mid D(B_x, X) \geq d\} = \left\{x \mid \frac{\sum \mu_{B_x \wedge X}}{\sum \mu_B} \geq d\right\} \supseteq \left\{x \mid \frac{\sum \mu_{B_x \wedge Y}}{\sum \mu_B} \geq d\right\} \\ &= \{x \mid D(B_x, Y) \geq d\} \\ &\equiv T_Y\end{aligned}$$

implying that  $\underline{T_X \supseteq T_Y}$ , where inclusion follows from relation  $Y \preceq X$  due to the anti-extensive property of operator  $\theta_{B,d}$ . Now we prove that actually  $\underline{T_X = T_Y}$ . Using Eq. (5) we can write:

$$\begin{aligned}\forall y \in T_Y, \quad B_y \wedge Y &= B_y \wedge \left( \bigvee_{X \in T_X} (B_x \wedge X) \right) = B_y \wedge \left( \bigvee_{X \in T_X} B_x \right) \wedge X \\ &= \bigvee_{X \in T_X} (B_x \wedge B_y) \wedge X\end{aligned}$$

since  $y \in T_Y \subseteq T_X$  we have,

$$\begin{aligned}B_y \wedge Y &= \bigvee_{x \in T_X, x \neq y} (B_x \wedge B_y) \vee (B_{x=y} \wedge B_y) \wedge X = \bigvee_{x \in T_X, x \neq y} (B_x \wedge B_y) \vee B_y \wedge X \succeq B_y \wedge X \\ &\Rightarrow \forall y \in T_Y, \quad \underline{(B_y \wedge Y) \succeq (B_y \wedge X)},\end{aligned}$$

where the last inequality follows from Eq. (3). On the other hand,

$$Y \preceq X \Rightarrow \underline{(B_y \wedge Y) \preceq (B_y \wedge X)}.$$

Therefore, we can conclude that:

$$\forall y \in T_Y, \quad \underline{(B_y \wedge Y) = (B_y \wedge X)}. \quad (35)$$

From Eq. (35) it follows that:

$$T_Y = \left\{ y \mid \frac{\sum \mu_{B_y \wedge Y}}{\sum \mu_B} \geq d \right\} = \left\{ y \mid \frac{\sum \mu_{B_y \wedge X}}{\sum \mu_B} \geq d \right\} = T_X$$

$$\Rightarrow \underline{T_Y = T_X}. \quad (36)$$

Finally, using Eqs. (35) and (36), we can show that:

$$Z = \theta_{B,d}(Y) = \bigvee_{y \in T_Y} (B_y \wedge Y) = \bigvee_{y \in T_X} (B_y \wedge X) = \theta_{B,d}(X) = Y$$

$$\Rightarrow \underline{Z = \theta_{B,d}(Y) = Y},$$

and therefore the operator is idempotent.

## B Implementation issues

All computational experiments were carried out using a Matlab 6.5 tool installed on 3.2-GHz Pentium 4 PC.

### B1. Density opening operator

Density opening was implemented by the algorithm 1.

---

**Algorithm 1** Implementation of density opening  $Y = \theta_{B,d}(X)$

---

1. Convolution of initial image with symmetric SE B  
Fuzzy set(densities)  $X_1 = \{(x, \mu_{x_1}(x)) \mid x \in E\}$ ,  
 $\mu_{x_1}(x) = \mu_x(x) * \frac{\mu_B(x)}{|B|}$
  2. Thresholding of  $X_1$  at level defined by density parameter  
The crisp set(marker)  $X_2 = \{x \mid \mu_{x_1}(x) \geq d\}$
  3. Dilation of marker  $X_2$  by SE B  
Crisp set(mask)  $X_3 = X_2 \oplus B$
  4. Generation of opened image  $Y$  by saving initial image under mask  $X_3$  and elimination of the remained parts  
Fuzzy set  $Y = \{(y, \mu_Y(y)) \mid y \in E\}$ ,  
 $\mu_Y(y) = \begin{cases} \mu_x(y), & \text{when } y \in X_3 \\ 0, & \text{when } y \notin X_3 \end{cases}$
- 

Density opening can be implemented in other ways. For example, density opening of a binary image can be implemented using a rank filter to define a marker (Stage 2). However, this method is generally slower. To get some idea of the times required for

calculation of density opening in Matlab, we use the binary and gray-tone images in Figs. 9(a) and 10(a) of  $150 \times 150$  in size and operator  $\theta_{r,d}$  with parameters  $r = 10$ ,  $d = 0.6$ . The time required for opening of the binary image in Fig. 9(a) was 0.047 s and for opening of the gray-tone image in Fig. 10(a) was 0.156 s.

## B2. Size and density spectra

Density opening with a large SE is time-consuming (as for structural opening). For example, density opening of the gray-tone image in Fig. 10(a) of  $150 \times 150$  in size by a disk of radius 30 ( $r = 30$ ) and density equal to 0.6 ( $d = 0.6$ ) requires 0.781 s. It is possible to speed up the process by sampling the initial image. Sampling is performed only for openings with large SE. In this case we lose minimal image information and considerably speed up the opening. Practical generation of top-hat pattern spectra becomes more complicated, however. We sampled an image by powers of two:  $I \downarrow 2^n$ , where  $n = \lfloor \frac{r}{s} \rfloor$ ,  $\lfloor \cdot \rfloor$  is a whole part of the division,  $r$  is the SE size and constant  $s$  was selected to be 30.

## B3. Some technical details related to the classification experiments

The size-density signatures in classification experiments were generated on the following grid:  $d = [0.1 : 0.02 : 1]$ ,  $r = [0 : 1 : 30, 32 : 2 : 60, 64 : 4 : 120, 128 : 8 : 144]$ . We use a disk structuring element, comprising all pixels whose centers are at a distance of no more than  $r$  from the origin. In the experiment with artificial images, the 1D vectors that were supplied to SVM (after column-wise signature scanning and feature selection as described in Section 6.), contained approximately 1700 entries for type 1 signatures and 1900 entries for types 2 and 3 signatures. In the experiment with real world medical images, 1D feature vectors contained 2419 entries. For classification purposes, the LIB-SVM tool [21] was used with a radial basis function (RBF) kernel. In the experiment with artificial images, acceptable kernel parameters  $\gamma$  and the C-parameter were selected to be 0.0039 and 32, respectively. Selection was based on the cross-validation procedure. The image test set was not used for selection of the SVM parameters or for training of the SVM. In the experiment with real world medical images a two-stage cross validation procedure was used [22]. First the data is divided into a training set and a validation set. Next, a cross-validation (CV) procedure is applied within the training set in order to determine the SVM hyper-parameters in a standard fashion. Then, the SVM classifier with the selected hyper-parameters is used in order to classify the validation set, yielding the final assessment of the error. This procedure is repeated several times, and the final error assessment is given by averaging the results. This two-stage CV procedure allows one to use all data for both testing and training the classifier, while providing an unbiased assessment of the error. We used 10-fold CV for both the external and internal loops.

**Acknowledgments** The authors are very grateful to Dr. Renato Keshet for his assistance throughout the research period and for his insightful remarks about the paper.

## References

- [1] P.Maragos, Pattern spectrum and multiscale shape representation, IEEE Transactions on Pattern Analysis and Machine Intelligence. July 1989; 11(7): 701-16
- [2] R.A. Peters, Morphological pseudo bandpass image decompositions , SPIE-Int. Soc. Opt. Eng. Journal of Electronic Imaging. April 1996; 5(2): 198-213
- [3] P.Soille, On morphological operators based on rank filters, Elsevier,Pattern Recognition.2002:527-535
- [4] P.Soille, Morphological Image Analysis, Springer 2003.
- [5] M.H.F Wilkinson, Generalized pattern spectra sensitive to spatial information , IEEE Comput.Soc, Proceedings 16th International Conference on Pattern Recognition. 2002: 21-4 vol.1
- [6] J.Van Horebeek, E.Tapia Rodriguez,The approximation of a morphological opening and closing in the presence of noise ,Elsevier, Signal Processing. Sept. 2001; 81(9): 1991-5
- [7] M.Vanrell. J.Vitria, Mathematical morphology, granulometries and texture perception , Proceedings of the SPIE International Society for Optical Engineering. 1993; 2030: 152-61
- [8] J.Serra, Image Analysis and Mathematical morphology. Academic Press,1982
- [9] J.Serra, Image analysis and mathematical morphology. vol2. Theoretical advances, Academic Press, London, 1988.
- [10] P.Kuosmanen, J.Astola Soft morphological filtering,J.of Math. Imaging and Vision,1995:231-262
- [11] C.Ronse, Erosion of narrow image features by combination of local low rank and max filters, in Proc.2nd Int. Conf. on Image Processing and its applications, London, 1986, pp 77-81
- [12] G.Ayala, J.Domingo, Spatial size Distributions: Applications to Shape and Texture Analysis, IEEE Trans. on Pattern Anal. and Machine Intellegence,Vol 23,N12,2001
- [13] G.Matheron, Random sets and Integral Geometry, New York:Wiley, 1975
- [14] P.J. Burt E.H Adelson, The laplacian pyramid as a compact image code, IEEE Trans. Commun, Vol 31 , pp 532-540, Apr 1983

- [15] S.R Sternberg, Grayscale morphology, *Comput. Vision, Graph, Image Processing*, vol.35 pp. 333-355, 1986
- [16] R.M Haralick, S.R Sternberg, and X.Zhuang, Image analysis using mathematical morphology, *IEEE Trans. Pattern anal. Machine Intell.*, vol. PAMI-9, pp. 523-550, July 1987
- [17] Y.Nakagawa and A.Resenfeld, A note on the use of local min and max operators in digital picture processing, *IEEE trans. Syst., Man, Cybern.*, vol. SMC-8, pp. 632-635, Aug 1978
- [18] V.N. Vapnik, *The nature of statistical learning theory*, Springer Verlag, New York, 1995
- [19] Muller K. Mika S. Ratsch G. Tsuda. K. Scholkopf B., An introduction to kernel-based learning algorithms, *IEEE-Transactions on Neural Networks*. March 2001; 12(2): 181-201
- [20] H.Heijmans, *Morphological image operators*, *Advnces in Electronics and Electron Physics*, Academic Press, Boston,1994
- [21] C.Chang and C.Lin, *LIBSVM: A Library for Support Vector Machines*,2001. Software available at <http://www.csie.ntu.edu.tw/~cjlin/libsvm>
- [22] I.Zingman, *Analysis and classification of tissue section images*, M.Sc. Thesis, Technion, January 2006
- [23] D.Sinha, E.Dougherty, A general axiomatic theory of intinsically fuzzy mathematical morphologies. *IEEE Trans. on Fuzzy Systems*, Vol 3, N 4, November 1995.
- [24] I.Bloch,H.Maitre, *Fuzzy Mathematical Morphologies: A comparative study*, *Pattern Recognition*, Vol 28, N 9, 1995